Synthesis of Micro-/Nanohydroxyapatite Assisted by the Taylor−Couette Flow Reactor

Boyin Wang and Shengyang Tao*

Read Online

ACCESS | Metrics & More | Article Recommendations | Supporting Information

ABSTRACT: Hydroxyapatite (HAP) has received increasing attention as an essential chemical product with good biocompatibility and adsorption properties. Generally, amorphous calcium phosphate (ACP) was generated first in the reactor and transformed into HAP after a period of crystallization. In this work, a series of Taylor−Couette flow reactors with different inner diameters were designed to assist in synthesizing HAP micro-/nanocrystals. ACP was obtained in a Taylor−Couette flow reactor at Re = 247 and successfully transformed into needle-like HAP crystals with a length of about 200 nm and a uniform particle size distribution after crystallization transformation. The yield of a single reactor can reach 2.16 kg per day. The finite element analysis results and time−space diagram of flow pattern variation showed that the Taylor−Couette flow reactor could improve the mixing behavior and the flow field distribution. The Taylor−Couette flow reactor provides a valuable reference for synthesizing inorganic micro-/nanomaterials.
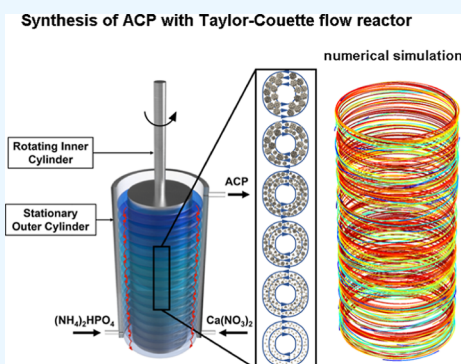
INTRODUCTION

Reactive precipitation is an essential method for synthesizing inorganic micro-/nanomaterials and has the advantages of simplicity and efficiency.[1] It usually consists of two steps: mixing and reaction. Since most precipitation reactions are instantaneous processes, mixing becomes the rate-control step of reactive precipitation.[2,3] The contributory factors in the precipitation process are the supersaturation of the solution[4] and the concentration distribution.[5] The supersaturation of the solution is affected by the concentration of the reactants.[6] It is the driving force of the precipitation reaction.[7] The transfer process influences the homogeneity of the concentration distribution during the mixing process in the reactor. Therefore, a significant transfer coefficient will result in better mixing performance. There are two main types of reactors commonly used for precipitation generation. One is the stirred reactor,[8] which has a large flux per unit time, but there is a dead zone in the stirring process[9] which makes the velocity field distribution inhomogeneous,[10] so the mixing effect is not ideal.[11] Moreover, differences in experimental conditions between batches will lead to differences in products,[12] especially when the reactor is scaled up. Therefore, continuous flow synthesis[13] has been invented to enhance the mixing,[14] such as microreactors.[15] The shrinkage of the overall size reduces macroscopic mixing inhomogeneity, resulting in a more uniform velocity field distribution and a better mixing effect.[16] However, the low flux of the microreactor will lead to low yields.[17] Moreover, the microchannels are easily blocked by the precipitate formed during the reaction. Therefore, it is necessary to develop a new type of reactor that combines the

advantages of these two reactors to increase the flux while maintaining homogeneous mixing.

As a secondary flow with an excellent mixing effect, the Taylor vortex flow was first discovered by G. I. Taylor[18] in 1923. Since then, the Taylor−Couette flow reactor has come into being. It usually consists of two coaxial cylinders. The inner cylinder rotates while the outer cylinder is fixed,[19] and the inner and outer cylinder gap is the reaction site.[20] When the inner cylinder rotates at a certain speed, Taylor vortex flow will appear in the gap, and the impact jet area formed between the opposite rotating ring Taylor vortex enhances the mass transfer and facilitates mixing.[21] The simple structure and flexible operation have facilitated Taylor−Couette flow reactors' experimental and industrial development. Recently, many researchers have focused their interest on mixing enhancement in Taylor−Couette flow reactors. Moreover, to achieve continuous flow synthesis, inlets and outlets were added to the sidewalls of the reactor. In this way, the continuous flow of fluid creates an axial advection flow in the reactor, which results in a more uniform velocity field distribution and better mixing.

Judat et al.[5] proposed the concept of macro- and micromixing based on the precipitation of BaSO4 particles.
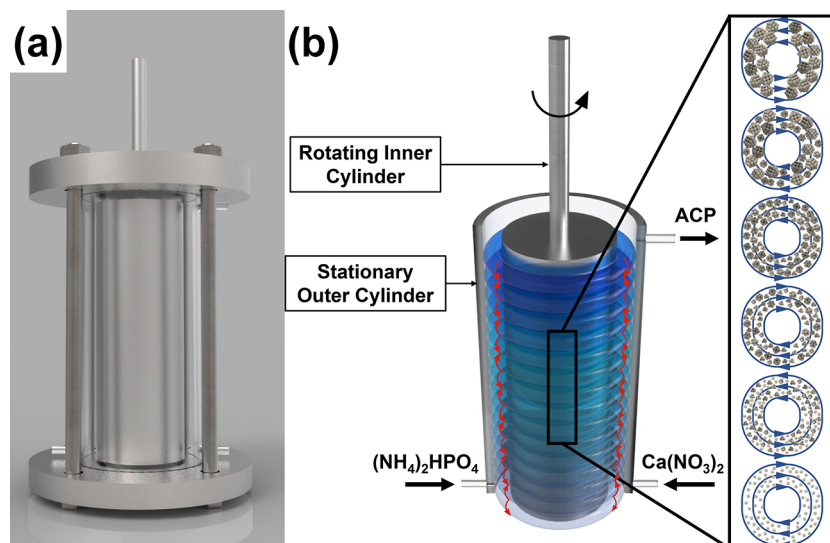
Figure 1. Schematic diagram of (a) Taylor−Couette flow reactor and (b) ACP nanoparticles prepared by the Taylor−Couette flow reactor.

They found that the $BaSO_4$ particle morphology was controlled by macromixing, and the particle size was mainly controlled by micromixing. AlAmer et al.[22] used a Taylor−Couette flow reactor for a continuous process of graphite flake oxidation and reduced the synthesis time of graphite oxide from hours to minutes in the Taylor vortex flow regime (TVF). Love et al.[23] used a Taylor−Couette flow reactor for continuous electrochemical synthesis and experimentally demonstrated that the Taylor vortex enhanced fluid mixing in the annular gap between electrodes, thus improving the selectivity of target products. The agglomeration process of nickel-rich hydroxide $(Ni_{0.9}Co_{0.05}Mn_{0.05})(OH)_2$ in a continuous Couette−Taylor crystallizer was studied by Thai et al.[24] The excellent mixing and periodic flow of the Taylor vortex promote the formation of spherical, homogeneous agglomerated particles. Kim et al.[25] investigated the effect of the Taylor vortex on the crystallization process of the gas−liquid reaction of calcium carbonate and found that the Taylor vortex enhanced the mass transfer at the gas−liquid interface, thus increasing the crystallization yield. These studies show that Taylor−Couette flow reactors exhibit great advantages in synthesizing inorganic micro-/nanoparticles.

As an important chemical product with good biocompatibility and adsorption properties, HAP has been widely used in biomedical,[26] chemical,[27] material,[28] environmental,[29] energy,[30] and other fields. Meyer's study[31] showed that HAP is formed from amorphous calcium phosphate (ACP) under alkaline conditions after a limited and highly reproducible period of crystallization transformation. In this work, the mixing properties of the Taylor−Couette flow reactor were investigated through the assisted synthesis of HAP, focusing on the regulation of the flow field state to make the initially generated ACP with small particle size and a uniform distribution. The results of experiments and numerical simulations show that the Taylor−Couette flow reactor has a strong mixing capacity. Furthermore, the ACP produced in this flow field state results in a regular shape, a small size, and a uniform distribution of HAP produced by the crystallization transformation.

MATERIALS AND EXPERIMENTAL METHODS

Materials. $Ca(NO_3)_2$ and $(NH_4)_2HPO_4$ were purchased from Beijing Chemical Reagent Company, $NH_3·H_2O$ and Glycerol were purchased from Kemiou Chemical Reagent Co. Ltd. All chemicals were not purified further.

Design of Taylor−Couette Flow Reactors. The schematic diagram of the Taylor−Couette flow reactor setup is shown in Figure 1a. The inner cylinder is made of stainless steel, and the outer cylinder is made of quartz glass with two inlets on the lower side and one outlet on the upper side. The inner diameter of the outer cylinder is 80 mm and the height is 170 mm. "A rotating inner cylinder and stationary outer cylinder" strategy was used in this study, and the dimensions of the reactor are shown in Table S1. Silicon rubber is used for sealing treatment, and silicon nitride ceramic bearings are used to support both ends of the inner cylinder to reduce the rotary resistance so that the inner cylinder can rotate at high speed. In order to investigate the effect of the gap width on the flow field state, five different diameters of inner cylinders were designed.

Assisted Synthesis of HAP. There are two main steps in the preparation of HAP. First, $Ca(NO_3)_2$ and $(NH_4)_2HPO_4$ solution, both at pH 10.5, were pumped into the rotating Taylor−Couette flow reactor from two inlets to produce ACP. Then the HAP was produced by crystallizing the ACP exiting from the reactor for 24 h.[17,32] The chemical equation for the reaction of $(NH_4)_2HPO_4$ with $Ca(NO_3)_2$ to generate HAP is shown in eq 1.

$$6(NH_4)_2HPO_4 + 8OH^- + 10Ca(NO_3)_2 \rightarrow Ca_{10}(PO_4)_6$$
$$(OH)_2 + 20NO_3^- + 12NH_4^+ + 6H_2O \tag{1}$$
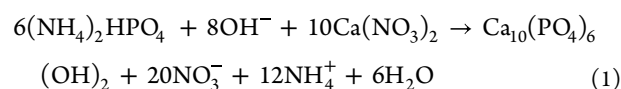
The pHs of $(NH_4)_2HPO_4$ solution and $Ca(NO_3)_2$ solution were adjusted to 10.5, and then pumped into the Taylor−Couette flow reactor with two peristaltic pumps at a flow rate of 3:7 from each of the two inlets to mix thoroughly. ACP gradually nucleated, aggregated, and grew under the mixing of Taylor vortices. Figure 1b is a schematic diagram of the Taylor−Couette flow reactor to prepare ACP. After a retention period in the reactor, ACP with a stable presence and uniform dispersion was received from the outlet. The sample was taken at 200 s from the moment of injection, and 60 mL of the

sample was taken in a 100 mL beaker. 10 μL of the sample was immediately taken in a 10 mL centrifuge tube and diluted to 10 mL with deionized water. After shaking well, 1 mL of the dilution was placed in the cuvette of the particle sizer to measure the particle size and distribution of the sample. The quality of HAP was influenced by its precursor, ACP, so we could obtain the relative size of HAP by examining the particle size of ACP.

The remaining solution in the beaker was aged for 24 h under stirring with a 2 cm C-type magnet, and the stirring speed was set to 1000 rpm. After aging, the impurity ions remaining on the sample surface were washed off by centrifugation-dispersion-centrifugation and then freeze-dried for 24 h to obtain white powders. The white powders were taken for specific surface area measurements and X-ray diffraction analyses.

The factors that may affect the size and distribution of HAP particle size are mainly concentration, inner cylinder diameter and rotational speed, and retention time. Therefore, these three factors will be mainly considered in this study.

Four different concentrations were investigated first. Then, a series of experiments were performed to investigate the effect of inner cylinder diameter (60−76 mm) and rotational speed (600−1800 rpm). The effect of retention time (0.5−5.5 min) on ACP particles' size and distribution was investigated.

Flow State Exploration. In order to observe the flow state in the Taylor−Couette flow reactor more visually,[33] pearl powder was added to the aqueous glycerol solution as tracer particles. The stirrer increases the speed at an incremental dRe/dt = 1.793 s^{-1}. The process was recorded using a Sony IMX 586 camera with a video frame rate of 240 fps.

Finite Element Analysis Simulation. COMSOL Multiphysics 5.3 was used for simulation to study the process of diffusion and mixing in the Taylor−Couette flow reactor and impeller stirrer. The fluid was assumed to be incompressible. Many key simulation parameters came from experiments, as shown in Table S2. The mesh parameters of the numerical simulation models are shown in Table S3. A frozen rotor study was used to calculate the flow velocity at a steady-state, and the Navier−Stokes equations were used to study the fluid flow, as shown in eqs 2 and 3. Where u is the velocity vector, ρ is the density of the fluid, μ is the viscosity, p is the pressure, and F is a body force term, such as gravity. The initial value of all simulated velocities was set to 0 m/s. The rotational speed of the rotational domain was set according to Table S6, and the PARDISO solver was selected.

$$\rho(\boldsymbol{u}\cdot\nabla)\boldsymbol{u} = \nabla\cdot[-p\boldsymbol{I} + \mu(\nabla\boldsymbol{u} + (\nabla\boldsymbol{u})^T)] + \boldsymbol{F} \tag{2}$$

$$\rho\nabla\cdot\boldsymbol{u} = 0 \tag{3}$$

Characterization. An Anton Paar Litesizer 500 laser particle sizer measured the particle size and distribution. The specific surface area of the powders was measured with a Quantachrome Instruments specific surface area tester. A Rigaku D/MAX-2400 X-ray diffractometer, Japan, analyzed the crystal structure. Transmission electron microscopy was performed with a Tecnai F30 electron microscope equipped with a Schottky field emission gun (FEG) (300 kV accelerating voltage). The viscosity of the liquid was measured with the SNB-2 digital viscometer.

RESULTS AND DISCUSSION

Effect of Concentration. The effect of concentration was explored to investigate the formation kinetics of ACP, the precursor of HAP. Four different concentrations of solutions were prepared, and their concentrations and volumes are shown in Table S4.

The inner cylinder diameter of the Taylor−Couette flow reactor was 74 mm, and the rotational speed was set to 1200 rpm. As shown in Figure 2a, with the increase in solution
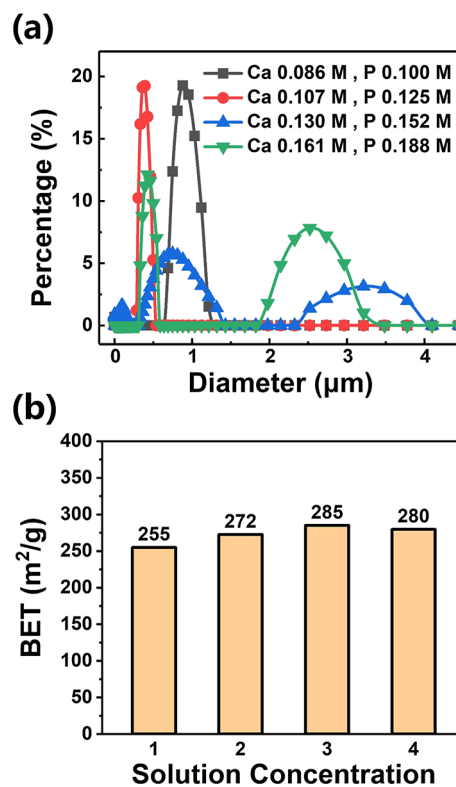

Figure 2. (a) Particle size and distribution of ACP prepared at four different concentrations. (b) Specific surface area of HAP at four different concentrations.

concentration, the particle size of the sample decreased and then increased, and the monodispersity got better and then worse. The smallest particle size and the best monodispersity of the samples were obtained at a concentration of 0.107 M for $Ca(NO_3)_2$ and 0.125 M for $(NH_4)_2HPO_4$.

The samples were aged, separated, and dried to obtain the white powder, identified as HAP after XRD image comparison in Figure S1.[34] From Figure 2b, the specific surface area of the white powder showed a slight variation overall, and all managed to be greater than 255 m^2/g.

Equation 4[35] is the classical nucleation theory

$$\Delta G = 4\pi r^2\gamma - \frac{4\pi r^3}{3M_r}RT\ln S \tag{4}$$

where γ is the specific surface energy, r is the nucleus radius, and S is the degree of supersaturation. From eq 4, it can be found that as the concentration of the solution increases, the supersaturation increases and the Gibbs free energy decreases, which facilitates spontaneous nucleation.[36] The formation of many nuclei is favorable for obtaining small particles in a limited time. It is consistent with the results obtained in Figure
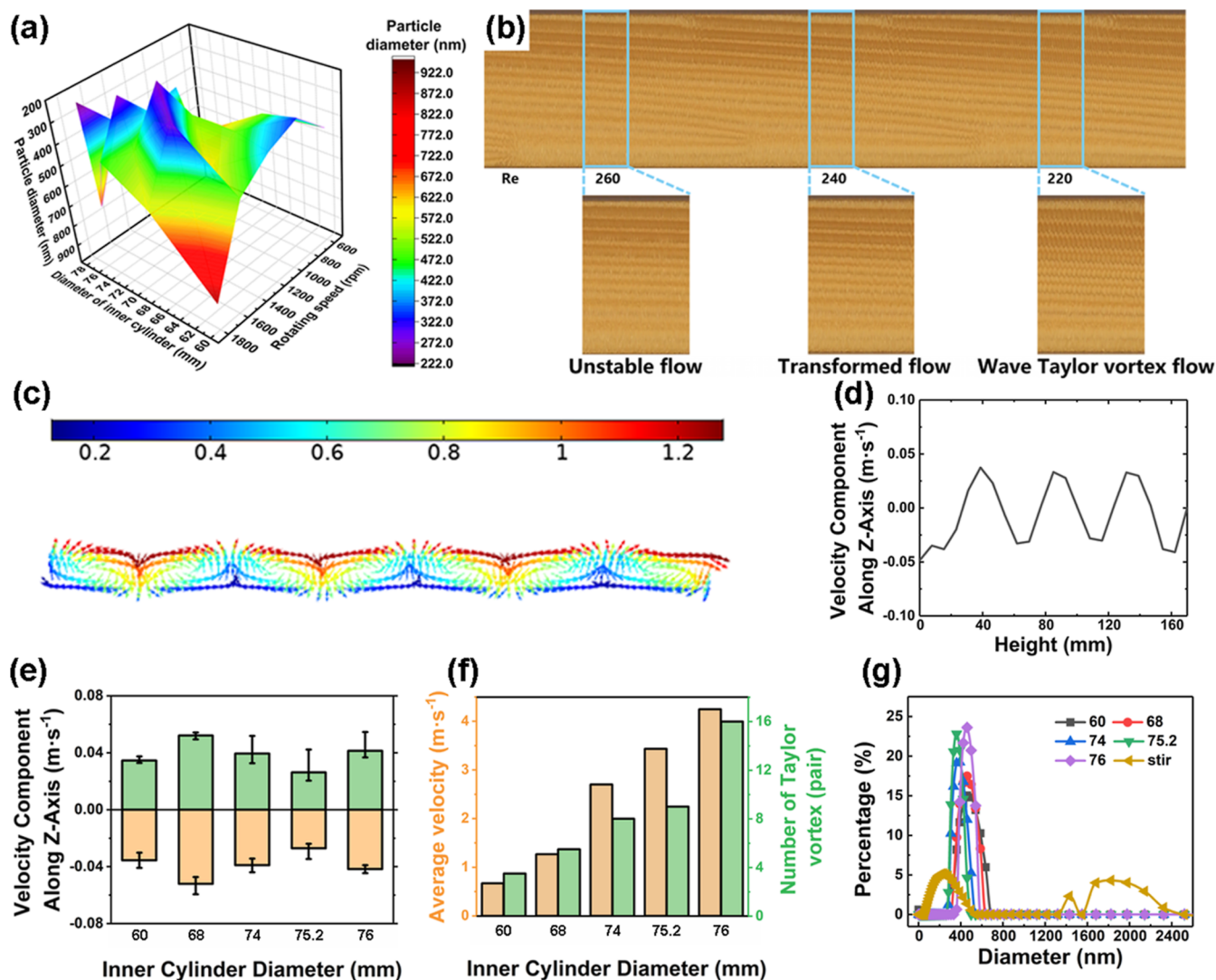
Figure 3. (a) Particle size of ACP at five rotational speeds (600, 900, 1200, 1500, and 1800 rpm) at five inner cylinder diameters (60, 68, 74, 75.2, and 76 mm). (b) Time−space diagram of flow pattern variation with increasing Reynolds number (mica pearl powder as the tracer particle). (c) Velocity field images and (d) axial velocity components of the inner cylinder edge line for Re = 247 in a 60 mm inner cylinder. (e) Axial velocity components of the inner cylinder edge line for Re = 247 and (f) average velocity and the number of Taylor vortexes at different inner cylinder diameters. (g) Particle size of ACP at Re = 247 under different conditions.

2b. The specific surface area and particle size of the samples did not change much with the increase in the solution concentration. However, the samples with 0.107 M $Ca(NO_3)_2$ and 0.125 M $(NH_4)_2HPO_4$ conditions had the smallest particle size and the best monodispersity. Therefore, subsequent experiments will be done based on this concentration for further studies.

Effect of Inner Cylinder Diameter and Rotational Speed. In order to investigate the effects of the inner cylinder diameter and rotational speed of the Taylor−Couette flow reactor on the particle size and distribution of ACP, a series of experiments, as shown in Table S5, were designed.[37]

Figure 3a shows the experimental results. As can be seen from the legend, the particle size corresponding to the blue-purple area is small. This study aimed to obtain HAP with a small particle size, so it was necessary to further explore the common points in the blue-violet region.

By comparison, it was found that the particle size distribution was small and uniform for the three groups of 74 mm, 1200 rpm; 75.2 mm, 1500 rpm; and 76 mm, 1800

rpm. It is well known that the Reynolds number is the most common dimensionless number used to describe the state of a fluid.[33] In many hydrodynamic problems, it determines whether fluid is in a laminar or turbulent state. As shown in formula 5,[38] the Reynolds number in a Taylor−Couette flow reactor is defined as

$$Re_T = \frac{R\omega d\rho}{\mu}$$

(5)

where R is the radius of the inner cylinder, ω is the speed of the inner cylinder, d is the width of the inner and outer cylinder gap, ρ is the fluid density, and μ is the dynamic viscosity of the liquid. The dynamic viscosity of the ACP suspension was measured to be 0.009 Pa·s. The Reynolds numbers corresponding to these 25 conditions are shown in Table S5. By comparison, the Reynolds number of these three better data sets was all around 247.

At a Reynolds number of 247, the rotational speeds corresponding to five different inner cylinder diameters are
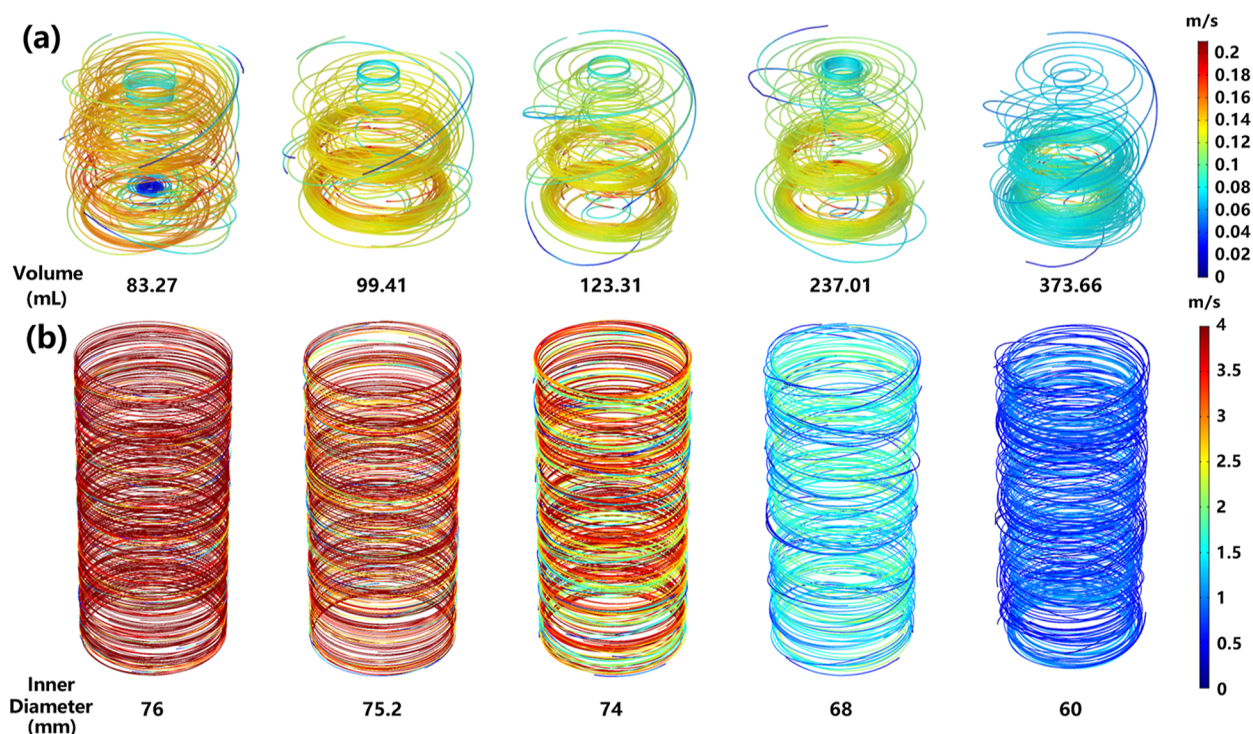
Figure 4. Velocity flow diagram for Re = 247. (a) Impeller stirrer. (b) Taylor−Couette flow reactor.

shown in Table S6. A further study was done on the five sets of parameters corresponding to Table S6. Meanwhile, as a control experiment, the rotational speed was adjusted according to the size of the impeller stirrer to achieve a Reynolds number of 247. As shown in formula 6,[39] the Reynolds number in the impeller stirrer is defined as

$$Re_I = \frac{\omega d^2 \rho}{\mu} \tag{6}$$

where ω is the impeller speed, d is the impeller diameter, ρ is the fluid density, and μ is the dynamic viscosity of the liquid. The diameter of the stirring impeller is 31.2 mm.

Combining Figure 3a and Table S5, it was clear that the blue-violet area corresponds to a Reynolds number around 247. Therefore, we supposed that the uniform flow field distribution at Reynolds number 247 was favorable for mixing, resulting in the product's small and uniformly distributed particle size.

To confirm this hypothesis, we pumped the aqueous glycerol solution with tracer particles into the Taylor−Couette flow reactor to investigate the variation of the fluid flow state. According to the space−time diagram[40] of flow pattern change with increasing Reynolds number shown in Figure 3b, it was clear that when the Re = 220, the fluid state was wavy Taylor vortex flow, and the boundary between adjacent Taylor vortices was discernible. When the Reynolds number increased to about 240, the wave-like features gradually disappeared, and the boundary became vague. Finally, when the Reynolds number increased to 260, the fluid destabilized, the boundary blurred, and the wave-like characteristics disappeared utterly.

Subsequently, the velocity field at Re = 247 was further investigated by numerical simulation. Figure 3c−e shows the velocity field images and the axial velocity component images of the inner cylinder edge line for five diameters at Re = 247. As shown in Figure 3e, the maximum value of the axial velocity

component of the inner cylinder edge line was stable at around 0.04 m/s with the increase in the inner cylinder diameter and rotational speed. The axial velocity component of the inner cylinder edge line directly reflected the magnitude of the vortex kinetic energy.[41] For different diameters of the inner cylinder, the vortex kinetic energy differed little even though the average velocity differed. Therefore, the mixing effect is comparable within the Taylor vortex cell at Re = 247, even if the inner cylinder diameters are different. As shown in Figure 3f, the average velocity and the number of Taylor vortex cells increased with the inner cylinder diameter. Details are shown in Figure S2. Combining the experimental and simulation results, it was clear that the fluid had the best mixing performance at a Reynolds number of around 240.

In order to compare the mixing properties of the Taylor−Couette flow reactor and impeller stirrer at the same Reynolds number, numerical simulations were conducted, and the results are shown in Figure 4. Under the condition of Re = 247, the velocity field of the impeller stirrer is not uniform, there is a dead zone, and the overall velocity is low.[9] In contrast, the Taylor−Couette flow reactor had a uniform velocity field distribution under Re = 247, and the velocities were all maintained at a high level. This result further confirmed the superior mixing performance of the Taylor−Couette flow reactor over the impeller stirrer.

Subsequently, the above numerical simulation results were experimentally verified. HAP was prepared in five Taylor−Couette flow reactors with different inner cylinders and one impeller stirrer under Re = 247 conditions. The sample was aged, separated, and dried to obtain a white powder, identified as HAP after the XRD image comparison in Figure S3. As shown in Figure 3g, with the increase of the inner cylinder diameter from 60 to 76 mm, the particle size of ACP ranged from 360 to 460 nm, and the monodispersity was good.
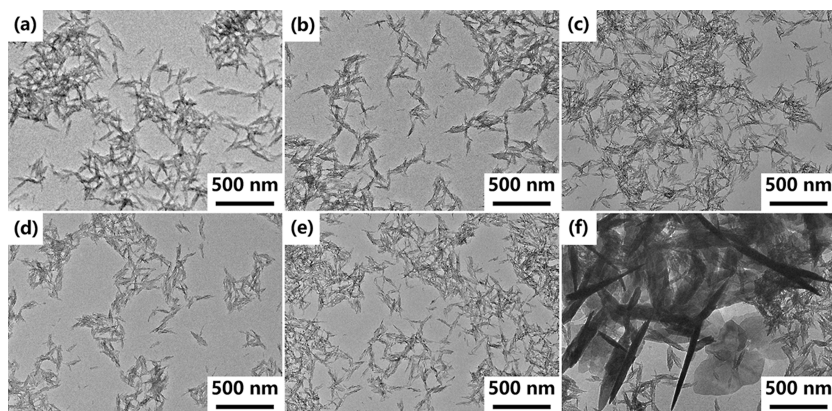
Figure 5. TEM images of HAP at Re = 247. (a) 60 mm inner cylinder. (b) 68 mm inner cylinder. (c) 74 mm inner cylinder. (d) 75.2 mm inner cylinder. (e) 76 mm inner cylinder. (f) Impeller stirrer.

However, the traditional impeller stirrer produced a product with poor dispersion and a great number of agglomerates.

Figure 5 showed the TEM images of HAP made under five different diameters of the inner cylinder and impeller stirrer. As shown in Figure 5, the HAP from the Taylor−Couette flow reactor was about 200 nm long needle-like crystals, while the product from the impeller stirrer had a significant number of large-sized crystals and amorphous products in addition to the above needle-like crystals. More details of the needle-like crystals can be seen in Figure S5.

The above experimental results demonstrate that the particle size of HAP from the crystallization of ACP prepared by the Taylor−Couette flow reactor was small and uniformly distributed when Re = 247. When Re = 247, the reactants were well mixed in the Taylor−Couette flow reactor, while in the impeller stirrer, the presence of dead zones made the mixing inhomogeneous, and part of the particles underwent abnormal growth while part was not converted into crystals in time.

In the Taylor−Couette flow reactor, when Re = 247, the fluid state was at a critical value for the disappearance of the wavy Taylor vortex. The reactants were well mixed without getting out of the Taylor vortex in this state. Thus, the products were separated from the outlet in time with the overall flow of the fluid. After the aging transformation, micro-/nano-HAP with a small particle size and a uniform distribution was obtained. According to previous studies, in a Taylor flow reactor, as the Reynolds number increases, the fluid state will experience the Couette flow, Taylor vortex flow, wavy Taylor vortex flow, and turbulent flow.[42,43] When the Reynolds number was in the Taylor vortex stage, although the boundary of the Taylor vortex could confine the particles inside the vortex well, it failed to mix the reactants sufficiently due to insufficient vortex kinetic energy, which led to the abnormal growth of some particles due to the excessive local supersaturation and makes the particle size distribution not uniform enough. When the Reynolds number was in the turbulent stage, although the vortex kinetic energy was sufficient to make the reactants thoroughly mixed, the wavy Taylor vortex boundary weakened the particles' binding effect. As a result, some nucleated products were tumbled to the lower part of the reactor, where the reactant concentration was higher, resulting in abnormal growth of some particles, which made the particle size distribution not uniform.

Effect of Retention Time. The effect of retention time (0.5−5.5 min) on the size and distribution of ACP particles was investigated at an inner cylinder diameter of 74 mm and a rotational speed of 1200 rpm. The flow rates of solutions corresponding to different retention times are shown in Table S7. All the flow ratios used in this section were $Ca(NO_3)_2$: $(NH_4)_2HPO_4$ = 7:3. The sampling time and operation steps are the same as in the previous section and will not be repeated here.

The particle size and distribution were measured with a particle size meter. Then the sample was aged, separated, and dried to obtain a white powder, identified as HAP after the XRD image comparison in Figure S4. The effect of retention time on particle size and distribution is shown in Figure 6.
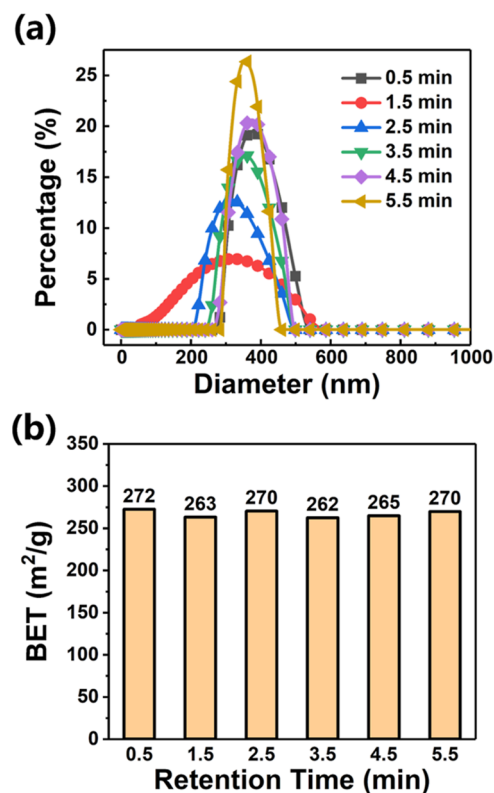

Figure 6. Effect of retention time on particle size distribution. (b) Specific surface area of HAP at different retention times.

From the particle size shown in Figure 6a, there was no noticeable change in the particle size and distribution of the resulting product with increasing retention time. As shown in Figure 6b, the specific surface areas of the products were in the range of 260−270 m^2/g. It indicated that the increase in retention time had less effect on the particle size and distribution of HAP. The precipitation nucleation reaction rate was faster, and the aging time was much greater than the precipitation nucleation time, so small changes in retention time within the reactor had a more negligible effect on the reaction results.

CONCLUSIONS

Based on the assisted synthesis of micro-/nano-HAP, the mixing properties of the Taylor−Couette flow reactor were investigated, and the optimal conditions for the synthesis of micro-/nano-HAP were explored. Three aspects were explored in terms of reactant concentration, inner cylinder diameter size, and rotational speed of the Taylor−Couette flow reactor, and retention time. The results showed that the Reynolds number had the most significant influence on the size and distribution of HAP particles, and other factors affected less. From the time−space diagram of flow pattern variation, it could be seen that when Re = 247, the fluid state in the reactor was at the critical value of wavy Taylor vortex disappearance. On the premise of ensuring sufficient material exchange within the Taylor vortex, the material exchange between two adjacent Taylor vortices is restricted to avoid the remixing phenomenon, thus avoiding the abnormal growth of some grains. As a result, the Taylor−Couette flow reactor can improve the mixing behavior well and make the flow field distribution more uniform in this condition. Thus, HAP crystals with a more uniform particle size can be obtained. Furthermore, we can extend this method to synthesize other inorganic micro-/nanomaterials, which provides a reference for the mass production of inorganic micro-/nanomaterials with homogeneous particle sizes.

ASSOCIATED CONTENT

ⓈI Supporting Information

The Supporting Information is available free of charge at https://pubs.acs.org/doi/10.1021/acsomega.2c05491.

> XRD images, simulation results, high-resolution TEM image, reactor dimensions, simulation parameters, mesh parameters, reactant concentrations, Reynolds numbers under different conditions, rotational speeds, and retention times (PDF)

AUTHOR INFORMATION

Corresponding Author

Shengyang Tao − *Frontiers Science Center for Smart Materials Oriented Chemical Engineering, Dalian University of Technology, Dalian 116024, China; State Key Laboratory of Fine Chemicals and Department of Chemistry, School of Chemical Engineering, Dalian University of Technology, Dalian 116024, China;* ⓞ orcid.org/0000-0002-0567-8860; Email: taosy@dlut.edu.cn

Author

Boyin Wang − *Department of Chemistry, School of Chemical Engineering, Dalian University of Technology, Dalian 116024, China*

Complete contact information is available at:
https://pubs.acs.org/10.1021/acsomega.2c05491

Author Contributions

B.W.: conceptualization, data curation, formal analysis, investigation, methodology, software, validation, visualization, and writing—original draft. S.T.: conceptualization, funding acquisition, project administration, resources, supervision, and writing—review and editing.

Notes

The authors declare no competing financial interest.

ACKNOWLEDGMENTS

REFERENCES

(1) Kim, Y. I.; Kim, D.; Lee, C. S. Synthesis and characterization of CoFe$_2$O$_4$ magnetic nanoparticles prepared by temperature-controlled coprecipitation method. *Physica B: Condensed Matter* **2003**, *337*, 42−51.

(2) Judat, B.; Racina, A.; Kind, M. Macro- and Micromixing in a Taylor-Couette Reactor with Axial Flow and their Influence on the Precipitation of Barium Sulfate. *Chem. Eng. Technol.* **2004**, *27*, 287−292.

(3) Cheng, Q.; Fang, H.; Cao, R.; Ma, Z.; Wang, S.; Xie, R.; Xia, H.; Wang, D. Interfacial self-assembly of nanoparticles into macroscopic, monolayered films. *Supramolecular Materials* **2022**, *1*.

(4) Tichit, D.; Layrac, G.; Gérardin, C. Synthesis of layered double hydroxides through continuous flow processes: A review. *Chem. Eng. J.* **2019**, *369*, 302−332.

(5) Flores, J. H.; da Costa, M. E. H. M.; da Silva, M. I. P. Effect of Cu-ZnO-Al$_2$O$_3$ supported on H-ferrierite on hydrocarbons formation from CO hydrogenation. *Chin. J. Catal.* **2016**, *37*, 378−388.

(6) Lai, W. H.; Wang, Y. X.; Wang, Y.; Wu, M.; Wang, J. Z.; Liu, H. K.; Chou, S. L.; Chen, J.; Dou, S. X. Morphology tuning of inorganic nanomaterials grown by precipitation through control of electrolytic dissociation and supersaturation. *Nat. Chem.* **2019**, *11*, 695−701.

(7) Maraghechi, H.; Rajabipour, F.; Pantano, C. G.; Burgos, W. D. Effect of calcium on dissolution and precipitation reactions of amorphous silica at high alkalinity. *Cem. Concr. Res.* **2016**, *87*, 1−13.

(8) Chemelewski, K. R.; Li, W.; Gutierrez, A.; Manthiram, A. High-voltage spinel cathodes for lithium-ion batteries: controlling the growth of preferred crystallographic planes through cation doping. *J. Mater. Chem. A* **2013**, *1*. DOI: 10.1039/c3ta13265j

(9) He, W.; Xue, L.; Gorczyca, B.; Nan, J.; Shi, Z. Experimental and CFD studies of floc growth dependence on baffle width in square stirred-tank reactors for flocculation. *Sep. Purif. Technol.* **2018**, *190*, 228−242.

(10) Liu, W. J.; Ma, C. Y.; Liu, J. J.; Zhang, Y.; Wang, X. Z. Continuous reactive crystallization of pharmaceuticals using impinging jet mixers. *AIChE J.* **2017**, *63*, 967−974.

(11) Srirugsa, T.; Prasertsan, S.; Theppaya, T.; Leevijit, T.; Prasertsan, P. Comparative study of Rushton and paddle turbines performance for biohydrogen production from palm oil mill effluent in a continuous stirred tank reactor under thermophilic condition. *Chem. Eng. Sci.* **2017**, *174*, 354−364.

(12) Wei, D.; Cheng, G.; Huang, K.; Fang, J.; Yan, B. Hydro-distillation condition adjustment for different material particle sizes: a method to increase batch-to-batch quality consistency. *Int. J. Food Sci. Technol.* **2018**, *53*, 1140−1148.

(13) Darr, J. A.; Zhang, J.; Makwana, N. M.; Weng, X. Continuous Hydrothermal Synthesis of Inorganic Nanoparticles: Applications and Future Directions. *Chem. Rev.* **2017**, *117*, 11125−11238.

(14) Wang, X.; Dong, Q.; Qiao, H.; Huang, Z.; Saray, M. T.; Zhong, G.; Lin, Z.; Cui, M.; Brozena, A.; Hong, M.; et al. Continuous Synthesis of Hollow High-Entropy Nanoparticles for Energy and Catalysis Applications. *Adv. Mater.* **2020**, *32*, No. e2002853.

(15) Kikkeri, R.; Laurino, P.; Odedra, A.; Seeberger, P. H. Synthesis of carbohydrate-functionalized quantum dots in microreactors. *Angew. Chem., Int. Ed. Engl.* **2010**, *49*, 2054−2057.

(16) Yang, L.; Xu, F.; Chen, G. Enhancement of gas-liquid mass transfer and mixing in zigzag microreactor under ultrasonic oscillation. *Chem. Eng. Sci.* **2022**, *247*.

(17) Ding, B.; Wang, Z.; Wang, X.; Yang, W.; Wang, S.; Li, C.; Dai, H.; Tao, S. Sr^{2+} adsorbents produced by microfluidics. *Colloids Surf. A Physicochem. Eng. Asp.* **2021**, *613*.

(18) Taylor, G. I. Stability of a Viscous Liquid contained between Two Rotating Cylinders. *Phil. Trans. R. Soc. Lond. A* **1923**, *223*, 289−343.

(19) Krishnaraj, K. P.; Nott, P. R. A dilation-driven vortex flow in sheared granular materials explains a rheometric anomaly. *Nat. Commun.* **2016**, *7*, 10630.

(20) Matsumoto, M.; Masuda, H.; Hubacz, R.; Horie, T.; Iyota, H.; Shimoyamada, M.; Ohmura, N. Enzymatic starch hydrolysis performance of Taylor-Couette flow reactor with ribbed inner cylinder. *Chem. Eng. Sci.* **2021**, *231*.

(21) Liu, L.; Yang, X.; Yang, J.; Li, G.; Guo, Y. Effect of hydrodynamic heterogeneity on micromixing intensification in a Taylor−Couette flow reactor with variable configurations of inner cylinder. *AIChE J.* **2021**, *67*. DOI: 10.1002/aic.17225

(22) AlAmer, M.; Lim, A. R.; Joo, Y. L. Continuous Synthesis of Structurally Uniform Graphene Oxide Materials in a Model Taylor−Couette Flow Reactor. *Ind. Eng. Chem. Res.* **2018**, *58*, 1167−1176.

(23) Love, A.; Lee, D. S.; Gennari, G.; Jefferson-Loveday, R.; Pickering, S. J.; Poliakoff, M.; George, M. A Continuous-Flow Electrochemical Taylor Vortex Reactor: A Laboratory-Scale High-Throughput Flow Reactor with Enhanced Mixing for Scalable Electrosynthesis. *Org. Process Res. Dev.* **2021**, *25*, 1619−1627.

(24) Thai, D. K.; Mayra, Q.-P.; Kim, W.-S. Agglomeration of Ni-rich hydroxide crystals in Taylor vortex flow. *Powder Technol.* **2015**, *274*, 5−13.

(25) Kim, W.-S. Application of Taylor Vortex to Crystallization. *J. Chem. Eng. Jpn.* **2014**, *47*, 115−123.

(26) Zou, Z.; Wang, L.; Zhou, Z.; Sun, Q.; Liu, D.; Chen, Y.; Hu, H.; Cai, Y.; Lin, S.; Yu, Z.; et al. Simultaneous incorporation of PTH(1-34) and nano-hydroxyapatite into Chitosan/Alginate Hydrogels for efficient bone regeneration. *Bioact. Mater.* **2021**, *6*, 1839−1851.

(27) Low, H. R.; Avdeev, M.; Ramesh, K.; White, T. J. Zinc hydroxyapatite catalyst for decomposition of 2-propanol. *Adv. Mater.* **2012**, *24*, 4175−4179.

(28) Deng, L.; Li, Y.; Zhang, A.; Zhang, H. Characterization and physical properties of electrospun gelatin nanofibrous films by incorporation of nano-hydroxyapatite. *Food Hydrocoll* **2020**, *103*.

(29) Wei, W.; Sun, R.; Jin, Z.; Cui, J.; Wei, Z. Hydroxyapatite−gelatin nanocomposite as a novel adsorbent for nitrobenzene removal from aqueous solution. *Appl. Surf. Sci.* **2014**, *292*, 1020−1029.

(30) Xiong, Z. C.; Zhu, Y. J.; Qin, D. D.; Yang, R. L. Flexible Salt-Rejecting Photothermal Paper Based on Reduced Graphene Oxide and Hydroxyapatite Nanowires for High-Efficiency Solar Energy-Driven Vapor Generation and Stable Desalination. *ACS Appl. Mater. Interfaces* **2020**, *12*, 32556−32565.

(31) Meyer, J. L.; Weatherall, C. C. Amorphous to crystalline calcium phosphate phase transformation at elevated pH. *J. Colloid Interface Sci.* **1982**, *89*, 257−267.

(32) Ferraz, M. P.; Monteiro, F. J.; Manuel, C. M. Hydroxyapatite nanoparticles: A review of preparation methodologies. *J. Appl. Biomater. Biomech.* **2004**, *2*, 74−80.

(33) Hai, M.; Zhang, Q.; Li, Z.; Cheng, M.; Kuehne, A. J. C.; Shi, F. Visualizing polymer diffusion in hydrogel self-healing. *Supramolecular Materials* **2022**, *1*. DOI: 10.1016/j.supmat.2022.100009

(34) Wang, D.; Deng, J.; Deng, X.; Fang, C.; Zhang, X.; Yang, P. Controlling Enamel Remineralization by Amyloid-Like Amelogenin Mimics. *Adv. Mater.* **2020**, *32*, No. e2002080.

(35) Li, C.; Ding, B.; Zhang, L.; Song, K.; Tao, S. 3D-printed continuous flow reactor for high yield synthesis of $CH_3NH_3PbX_3$ (X = Br, I) nanocrystals. *J. Mater. Chem. C* **2019**, *7*, 9167−9174.

(36) Wu, S.; Li, M.; Sun, Y. In Situ Synchrotron X-ray Characterization Shining Light on the Nucleation and Growth Kinetics of Colloidal Nanoparticles. *Angew. Chem., Int. Ed. Engl.* **2019**, *58*, 8987−8995.

(37) Razzak, M. A.; Khoo, B. C.; Lua, K. B. Numerical study on wide gap Taylor Couette flow with flow transition. *Phys. Fluids* **2019**, *31*, 113606.

(38) Majji, M. V.; Banerjee, S.; Morris, J. F. Inertial flow transitions of a suspension in Taylor−Couette geometryInertial flow transitions of a suspension in Taylor-Couette geometry. *J. Fluid Mech.* **2017**, *835*, 936−969.

(39) Wyrobnik, T. A.; Oh, S.; Ducci, A.; Micheletti, M. Engineering characterization of the novel Bach impeller for bioprocessing applications requiring low power inputs. *Chem. Eng. Sci.* **2022**, *252*.

(40) Ramesh, P.; Bharadwaj, S.; Alam, M. Suspension Taylor−Couette flow: co-existence of stationary and travelling waves, and the characteristics of Taylor vortices and spirals. *J. Fluid Mech.* **2019**, *870*, 901−940.

(41) Martinand, D.; Serre, E.; Lueptow, R. M. Mechanisms for the transition to waviness for Taylor vortices. *Phys. Fluids* **2014**, *26*, 094102.

(42) Dash, A.; Anantharaman, A.; Poelma, C. Particle-laden Taylor−Couette flows: higher-order transitions and evidence for azimuthally localized wavy vortices. *J. Fluid Mech.* **2020**, *903*, A20.

(43) Kang, C.; Mirbod, P. Flow instability and transitions in Taylor−Couette flow of a semidilute non-colloidal suspension. *J. Fluid Mech.* **2021**, *916*, A12.